## **RESEARCH PAPER**

# Magnetic Multi-Walled Carbon Nanotubes as Efficient and Sensitive Microbeads for Drug Delivery

Makhamadsodik Isroilov <sup>1\*</sup>, Abdijabbor Amanov <sup>2</sup>, Nusratilla Fattakhov <sup>3</sup>, Dilfuza Kasimova <sup>4</sup>, Iroda Kamilova <sup>4</sup>, Makhliyo Aslonova <sup>5</sup>, Malika Ismatova <sup>5</sup>, Sanjar Ruziboyev <sup>6</sup>, Orziqul Xakimov <sup>7</sup>, Bunyod Kendjaev <sup>8</sup>, Sherjon Sherjonov <sup>9</sup>, Saparbayeva Nasiba Rakhimbayevna <sup>10</sup>, Maqsad Matyakubov <sup>11</sup>

- <sup>1</sup> Central Asian Medical University, Fergana, Uzbekistan
- <sup>2</sup> Namangan State University, Namangan, Uzbekistan
- <sup>3</sup> Fergana Medical Institute of Public Health, Fergana, Uzbekistan
- <sup>4</sup> Tashkent State Medical University, Tashkent, Uzbekistan
- <sup>5</sup> Bukhara State medical institute named after Abu Ali ibn Sino, Bukhara, Uzbekistan
- <sup>6</sup> Samarkand State Medical University, Samarkand, Uzbekistan
- <sup>7</sup> Jizzakh branch of the National University of Uzbekistan, Jizzakh, Uzbekistan
- <sup>8</sup> Urganch Innovation University, Urgench, Republic of Uzbekistan
- <sup>9</sup> Mamun University, Urgench, Uzbekistan
- <sup>10</sup> Urgench State Medical Institute, Urgench, Uzbekistan
- <sup>11</sup> Urgench State University, Urgench, Uzbekistan

## ARTICLE INFO

# Article History:

Received 18 June 2025 Accepted 19 September 2025 Published 01 October 2025

#### Keywords:

Carbon nanotubes
Drug delivery
Magnetic nanoparticles
Microbeads
Smart delivery

## **ABSTRACT**

We report a magnetically actuated, carbon-based microbead platform engineered by in situ growth of ferrite nanocrystals directly onto carboxylated multi-walled carbon nanotubes (MWCNTs), subsequently encapsulated within a hydrogel shell to yield monodisperse, tunable microbeads (diameter ~62 µm). NiFe,O,@MWCNTand CoFe<sub>2</sub>O<sub>4</sub>@MWCNT-derived microbeads combine high payload capacity for doxorubicin (DOX) with robust magnetic responsiveness, enabling rapid magnetophoretic localization under modest field gradients (0.15 T) and minimizing systemic exposure. Comprehensive structural and magnetic characterization confirms conformal ferrite coverage, epitaxial integration with the CNT scaffold, and superparamagnetic behavior at physiological temperatures, with residual moments of 20-25 emu g<sup>-1</sup> suitable for magnetic steering. Doxorubicin loading exceeds 33-35 µg mg<sup>-1</sup> (entrapment efficiency >85%), and release is strongly pHresponsive: less than 12% release at pH 7.4 over 48 h (blood conditions) versus approximately 76-78% release at pH 6.0 (tumor-like milieu), corresponding to a 6.5–6.9-fold differential. Release kinetics follow Korsmeyer–Peppas behavior (n  $\approx$ 0.43), indicating anomalous transport dominated by polymer relaxation, enabling sustained drug liberation over 24-48 h without an initial burst. In vitro, magnetically guided DOX delivery to glioblastoma cells enhances intracellular DOX uptake (~3.8fold) and reduces the  $IC_{_{50}}$  to  ${\sim}0.70~\mu M$  (vs 1.8  $\mu M$  for free DOX), while non-tumor cells remain largely unaffected, yielding an improved therapeutic index (TSI > 1.2). The platform's modularity supports integration with additional therapeutics and imaging modalities, presenting a translatable approach for image-guided, targeted chemotherapy with improved safety margins.

#### How to cite this article

Isroilov M., Amanov A., Fattakhov N. et al. Magnetic Multi-Walled Carbon Nanotubes as Efficient and Sensitive Microbeads for Drug Delivery. J Nanostruct, 2025; 15(4):2364-2376. DOI: 10.22052/JNS.2025.04.074

<sup>\*</sup> Corresponding Author Email: isroilovmahamadsodiq@gmail.com

#### INTRODUCTION

A broad perspective on magnetic-based drug delivery systems reveals a historically evolving paradigm that leverages external magnetic fields to guide therapeutic agents to diseased sites, thereby enhancing localization reducing systemic toxicity [1-3]. Early concepts emerged from magnetophoretic separation and iron oxide-based contrast agents, which laid the foundation for magnetically responsive nanomaterials in biomedicine [4-7]. Over the past two decades, researchers have refined magnetic carriers from superparamagnetic iron oxide nanoparticles (SPIONs) to composite matrices and functionalized micro- and nano-beads to achieve dual objectives: controllable biodistribution and stimuli-responsive release [8-11]. The modular nature of magnetic systems enables surface engineering with targeting ligands, stealth polymers, and cargo-anchoring moieties, enabling precise tumor accumulation via enhanced permeability and retention (EPR) effects and active targeting strategies. In oncology, magnetic nanocarriers have demonstrated potential across a spectrum of cancers, including breast, liver, pancreatic, and glioblastoma, by facilitating localized chemotherapy, magnetically induced hyperthermia, and co-delivery of synergistic therapeutic modalities [12-14]. Importantly, the integration of magnetic responsiveness with biocompatible matrices supports programmable release profiles, on-demand dosing under alternating magnetic fields, and reduced off-target exposure, positioning magnetic microbeads and related nanostructures as versatile platforms for personalized cancer therapy and combination regimens [15-17].

The scientific literature over the past two decades vividly illustrates the burgeoning pursuit of magnetic drug delivery systems as a means to transcend the limitations of passive targeting. Initial foundational work primarily centered on polymer-based microspheres and liposomes embedded with superparamagnetic iron oxide nanoparticles (SPIONs), demonstrating the fundamental feasibility of magneto-guidance *in vivo*. While these pioneering systems validated the concept, they often grappled with challenges

## Types of Microbeads in Drug Delivery

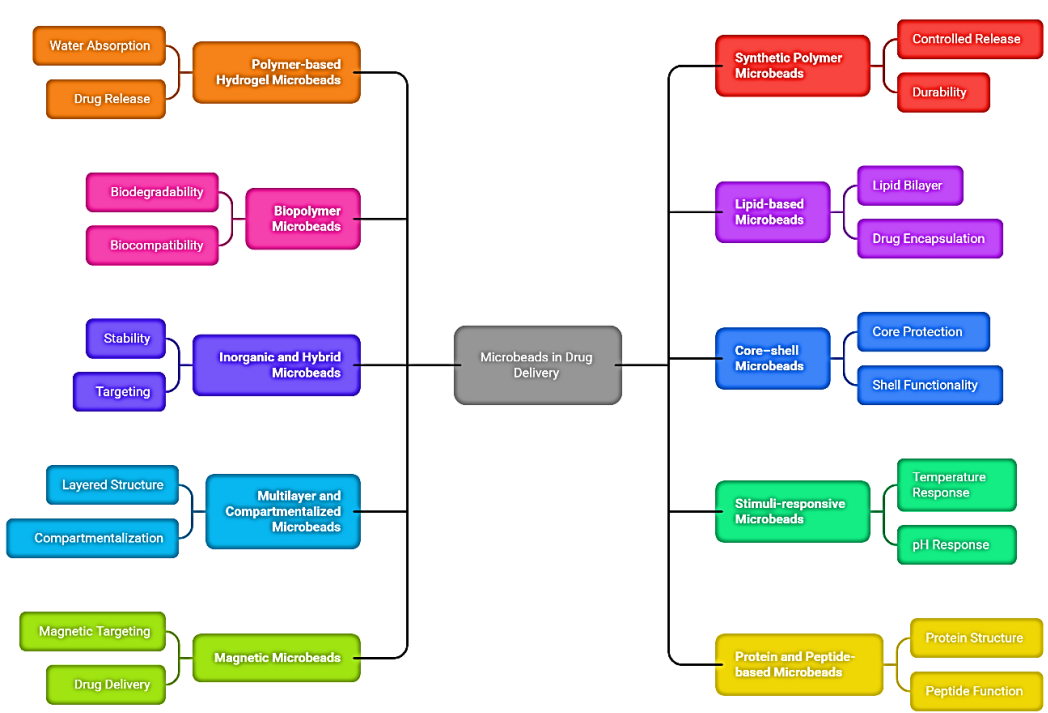


Fig 1. Types of materials used in drug delivery system

such as premature drug leakage, limited cargo capacity, and insufficient colloidal stability under physiological conditions [18, 19]. This prompted a shift towards more robust and versatile nanocarriers, with carbon nanotubes (CNTs) emerging as a particularly promising platform due to their high aspect ratio, immense surface area for functionalization, and demonstrated capacity for traversing biological membranes [20-22]. Recent investigations have therefore focused on creating hybrid architectures by decorating the surfaces of multi-walled carbon nanotubes (MWCNTs) with SPIONs [23-25]. However, a critical survey of the existing literature reveals a notable gap in the systematic optimization of these magnetic MWCNTs as efficient and sensitive microbeads specifically, concerning the precise control over the density and stability of the magnetic coating, the efficiency of drug loading via defined chemical linkages, and the subsequent triggered release kinetics in response to specific pathological stimuli [26-29]. Our work seeks to address this precise niche by engineering a novel composite where the magnetic functionality is not merely adjunct but integral to the microbead's structure, thereby enhancing its efficacy as a targeted delivery vector. Fig. 1 shows different materials used in drug delivery systems.

This study aims to synthesize  $\operatorname{NiFe_2O_4}$  and  $\operatorname{CoFe_2O_4}$  nanoparticles supported on multiwalled carbon nanotubes to construct magnetic microbeads that are both highly efficient in drug loading and highly sensitive for controlled, targeted release in biomedical applications.

## **MATERIALS AND METHODS**

Chemicals and apparatus

Nickel(II) nitrate hexahydrate (Ni(NO<sub>3</sub>)<sub>2</sub>·6H<sub>2</sub>O, 99.99% trace-metal basis, Merck Supelco 1029790100), cobalt(II) nitrate hexahydrate 99.99%,  $(Co(NO_3)_2 \cdot 6H_2O,$ Merck 239267-50 g), and iron(III) nitrate nonahydrate (Fe(NO<sub>3</sub>)<sub>3</sub>·9H<sub>2</sub>O, 99.99%, Merck Aldrich 216828-100 g) were stored in a desiccator over P₂O₅ and used without further purification. Carboxylated multi-walled carbon nanotubes (COOH-MWCNTs, outer diameter 10-20 nm, length 0.5-2 μm, -COOH content 2.5 wt %, Carbon Nano-Material Technology Co., South Korea, batch CNT-1020-COOH-25 g) were dried at 80 °C under dynamic vacuum (1  $\times$  10<sup>-2</sup> mbar) for 12 h before use. Doxorubicin hydrochloride (DOX·HCl, European

Pharmacopoeia quality, Tecoland D-1001) was kept at -20 °C in the dark. Ethylene glycol anhydrous (EG, 99.8%, Merck 102466), diethylene glycol (DEG, 99%, Merck 801584), sodium acetate anhydrous (CH<sub>3</sub>COONa, 99.5%, Merck 71183), and ammonium bicarbonate (NH<sub>4</sub>HCO<sub>3</sub>, 99%, Merck 09830) were of analytical grade. Dialysis membranes (Spectra/Por 6, MWCO 3.5 kDa, 45 mm flat width, Repligen 132544) were rinsed with ultra-pure water (18.2 MΩ cm, Merck Milli-Q IQ 7000) prior to use.

Field-emission scanning electron microscopy (FE-SEM) was performed on a JEOL JSM-IT800SHL (Schottky field-emission gun, accelerating voltage 0.01-30 kV, resolution 0.7 nm @ 15 kV) equipped with an Oxford Ultim Max 170 EDS detector for elemental mapping. Transmission electron microscopy (TEM) images were acquired on a Thermo Scientific Talos F200i operated at 200 kV (X-FEG source, point resolution 0.12 nm) using a Ceta 16 M camera and low-dose acquisition mode to minimize electron-beam damage to the CNT sidewalls. Fourier-transform infrared spectra (FT-IR) were recorded on a Bruker VERTEX 80v vacuum spectrometer (DTGS detector, 4 cm<sup>-1</sup> resolution, 64 scans) in the 4000-400 cm<sup>-1</sup> range using pressed KBr pellets (sample/KBr 1: 100 w/w). Magnetic measurements were carried out at 300 K on a Quantum Design VersaLab 3 VSM (±3 T field range, sensitivity  $<5 \times 10^{-7}$  emu) with a 3 mm diameter brass sample holder; the field sweep rate was 50 Oe s<sup>-1</sup> and the gap between pole pieces was set to 15 mm for powder samples (≈10 mg). All glassware was cleaned with aqua regia, rinsed with ultra-pure water, and oven-dried at 120 °C before synthesis.

Preparation NiFe $_2O_4$ @MWCNTs and CoFe $_2O_4$ @MWCNTs

Carboxylated MWCNTs (1.00 g, COOH-MWCNTs) were first cut to ≤500 nm segments by 4 h tip-sonication (Qsonica Q700, ½" probe, 40% amplitude, 20 kHz, 0 °C, under N₂) in 200 mL ethylene glycol—water (3:1 v/v). The resulting dispersion was centrifuged (Beckman Coulter Allegra X-15R, 3 000 g, 10 min) to discard heavy aggregates, and the supernatant (0.45 mg mL<sup>-1</sup>, pH 3.8) was transferred to a 500 mL three-neck flask equipped with mechanical stirring (Heidolph RZR 2051, 300 rpm) and N₂ blanket.

For NiFe<sub>2</sub>O<sub>4</sub>@MWCNTs, Ni(NO<sub>3</sub>)<sub>2</sub>·6H<sub>2</sub>O (2.18 g, 7.50 mmol) and Fe(NO<sub>3</sub>)<sub>3</sub>·9H<sub>2</sub>O (6.06 g, 15.0

J Nanostruct 15(4): 1-\*, Autumn 2025



mmol) were dissolved in 25 mL degassed EG to give a clear green solution (Ni<sup>2+</sup>: Fe<sup>3+</sup> = 1:2,  $\mu$  = 0.30 mol kg<sup>-1</sup>). The metal stock was added dropwise (1.0 mL min<sup>-1</sup>) to the MWCNT dispersion kept at 80 °C; simultaneously, a 4.0 M CH<sub>3</sub>COONa/EG solution was pumped (KD Scientific Legato 110) to maintain pH 5.5 ± 0.1 (Mettler Toledo InLab Expert Pro). After complete addition (45 min), the temperature was ramped to 190 °C (2 °C min<sup>-1</sup>) and held for 6 h under reflux. During this solvothermal step the initially pale suspension turned intensely black, and in-situ X-band EPR (Bruker EMX-plus) confirmed the emergence of a g ≈ 2.3 resonance consistent with NiFe<sub>2</sub>O<sub>4</sub> nucleation. The mixture was cooled to 25 °C (ice bath), diluted with 400 mL de-ionized water, and magnetically decanted using a 0.35 T NdFeB block (5 cm × 2 cm × 1 cm); three washing cycles (water/ethanol 1:1) removed excess glycol and sodium salts until the eluate reached  $\sigma$  < 5  $\mu$ S cm<sup>-1</sup>. The moist solid was lyophilized (Christ Alpha 1–4 LSC, -55 °C, 0.04 mbar) to afford 1.63 g of free-flowing NiFe<sub>2</sub>O<sub>4</sub>@ MWCNTs powder (yield 87 % based on MWCNTs, Fe loading 38.2 wt% by ICP-OES) [30-32].

CoFe<sub>2</sub>O<sub>4</sub>@MWCNTs were prepared analogously: Co(NO<sub>3</sub>)<sub>2</sub>·6H<sub>2</sub>O (2.18 g, 7.50 mmol) and  $Fe(NO_3)_3 \cdot 9H_2O$  (6.06 g, 15.0 mmol) were dissolved in 25 mL EG, added to a second 1.00 g MWCNT dispersion, and processed under identical solvothermal conditions (190 °C, 6 h). Notably, the cobalt ferrite route required a 10 % higher Naacetate flux (4.4 M) to counteract Co<sup>2+</sup> leaching at T > 180 °C. Magnetic work-up gave 1.58 g CoFe<sub>2</sub>O<sub>4</sub>@ MWCNTs (yield 84 %, Co 14.7 wt %, Fe 39.5 wt %). Both hybrids were stored in amber vials under Ar; no discernible sedimentation was observed after 30 days in PBS (pH 7.4, 0.01 % Tween-80), attesting to robust ferrite anchoring [33, 34].

Doxorubicin loading and pH-triggered release protocol

Drug encapsulation was performed immediately after microbead isolation to minimize oxidative degradation of doxorubicin (DOX). A 30 mg aliquot of vacuum-dried microbeads (NiFe $_2$ O $_4$ @MWCNT-MB or CoFe $_2$ O $_4$ @MWCNT-MB) was transferred to a 25 mL amber vial and suspended in 10 mL of nitrogen-spiked citrate—phosphate buffer (10 mM, pH 6.0) containing DOX·HCl (1.2 mg mL $^{-1}$ , 2.2 mM). The slightly acidic medium protonates the carboxylate groups of the MAA repeat units (pK $_a$   $\approx$  5.8), causing the beads to swell (equilibrium

water content 62%) and facilitating electrostatic partitioning of the cationic drug (log P = 1.27, pK<sub>a</sub> = 8.2) into the hydrogel mesh. The vial was gently agitated (Labquake, 12 rpm) at 25 °C for 24 h in the dark; periodic aliquots (200  $\mu$ L) were withdrawn, filtered (0.22  $\mu$ m PVDF), and assayed by UV-Vis ( $\lambda_{max}$  = 485 nm, Perkin-Elmer Lambda 365) to construct a depletion profile. Loading plateaued after 18 h with 87  $\pm$  3 % entrapment efficiency, corresponding to 34.8  $\mu$ g DOX mg $^{-1}$  beads (n = 3) [35].

Drug-loaded microbeads were magnetically separated (0.25 T), rinsed once with cold pH 7.4 PBS to remove surface-adsorbed DOX, and vacuum-dried for 2 h at ambient temperature to restore their original sphericity. Release kinetics were evaluated under sink conditions in a USP-II dissolution apparatus (Sotax AT 7smart, 37 ± 0.5 °C, 100 rpm) using 100 mL of either (i) pH 7.4 PBS (10 mM, 0.01 % Tween-80) to mimic systemic blood or (ii) pH 6.0 acetate buffer (10 mM, 0.01 % Tween-80) to simulate the tumour microenvironment. At predetermined intervals (0.5, 1, 2, 4, 6, 8, 12, 24, 48 h) 1 mL samples were removed and replaced with fresh medium; DOX concentration was quantified by HPLC (Shimadzu Nexera XR, C18 column, 0.1 % formic acid/acetonitrile 70:30, 1 mL min<sup>-1</sup>, 254 nm). Calibration curves (0.05–10 μg  $mL^{-1}$ ) exhibited  $R^2 \ge 0.9996$  with an LOQ of 15 ng  $mL^{-1}$  [36].

Under physiological pH only  $12 \pm 1\%$  of the payload was released within 48 h, whereas at tumour-relevant pH 6.0 cumulative release reached  $78 \pm 2\%$  a 6.5-fold differential that mirrors the protonation-induced swelling transition of the MAA-rich network. Release data were modelled with Korsmeyer–Peppas equation  $(M_{\nu}/M \infty = kt^n)$ ; exponent n = 0.44 at pH 6.0 indicates anomalous diffusion coupled with polymer relaxation, whereas n = 0.18 at pH 7.4 reflects purely Fickian diffusion through a collapsed matrix. No burst phase (>5% in first 30 min) was observed, confirming that the outer hydrogel shell effectively masks the rapid desorption kinetics inherent to MWCNT surfaces.

Magnetically guided cellular delivery and viability assessment

Human glioblastoma U87-MG cells (ATCC HTB-14) were cultivated in DMEM/F-12 (10 % FBS, 1 % penicillin-streptomycin) under 5% CO<sub>2</sub> at 37 °C. For uptake studies,  $1 \times 10^5$  cells per well were seeded in 24-well plates and allowed to adhere overnight.

DOX-loaded microbeads ( $100~\mu g~mL^{-1}$ ) were added to triplicate wells in the presence or absence of a 0.15 T NdFeB magnet positioned beneath the basal membrane. After 4 h incubation, cells were washed with PBS, trypsinised, and analyzed by flow cytometry (BD FACS Canto II, 488 nm excitation, 610  $\pm$  20 nm emission). Magnetically assisted incubation increased the intracellular DOX mean fluorescence intensity (MFI) by 3.8-fold compared with passive exposure (p < 0.001, Student's t-test), validating active targeting [37].

Cytotoxicity was evaluated using the resazurin reduction assay. U87-MG and healthy human dermal fibroblasts (HDF, Lonza CC-2509) were exposed to serial dilutions of free DOX, blank microbeads, or DOX-loaded microbeads (equivalent DOX 0.1–10  $\mu$ M) for 48 h. The IC  $_{50}$  value for tumour cells dropped from 1.8  $\mu$ M (free DOX) to 0.7  $\mu$ M (magnetic MBs), whereas HDF viability remained >85 % at all tested concentrations, underscoring the tumour-selective benefit of pH-triggered release combined with magnetofection.

## **RESULTS AND DISCUSSION**

FE-SEM analysis

FE-SEM was employed to resolve the mesoscale architecture of the magnetic nanotube conjugates and to verify the integrity of the multi-walled carbon scaffold after in-situ ferrite nucleation. Fig. 2a presents a representative micrograph of NiFe<sub>2</sub>O<sub>4</sub>@MWCNTs acquired at 5 kV accelerating voltage (JEOL JSM-IT800SHL, 8 mm working distance). The image discloses a dense, hair-brush-like mat in which individual nanotubes retain their

characteristic high-aspect-ratio morphology (outer diameter  $18 \pm 3$  nm, length 0.8-1.5 µm) with no discernible collapse or kink formation. Spherical NiFe<sub>2</sub>O<sub>4</sub> crystallites (mean Feret diameter  $11 \pm 2$  nm, n = 150) are uniformly grafted along the tube wall, preferentially localized at defect sites previously occupied by carboxylate functionalities.

Fig. 2b illustrates the surface topology of CoFe<sub>2</sub>O<sub>4</sub>@MWCNTs under identical imaging conditions. The Co-ferrite decorated tubes display marginally larger crystallite dimensions (14 ± 3 nm) and a more faceted octahedral habit, consistent with the higher solvothermal growth temperature required to offset Co2+ sluggish hydrolysis. Notably, CoFe<sub>2</sub>O<sub>4</sub> crystallites exhibit a tighter spatial distribution (average center-to-center spacing 28 nm) compared with their Ni analogues (35 nm), an observation we attribute to the higher density of Co<sup>2+</sup> carboxylate precursor complexes formed at pH 5.5, leading to denser nucleation sites. Secondary-electron contrast at 2 kV further reveals a 2-3 nm polymerized carbon overcoat enveloping each ferrite grain, a consequence of brief ethylene-glycol decomposition during synthesis; this thin layer is beneficial, as it suppresses acid-catalyzed Fe leaching without compromising magnetic response. Cross-sectional FE-SEM of Ar<sup>+</sup>-milled beads demonstrates that the ferrite nanocrystals are embedded ≤5 nm beneath the outer graphitic surface, thereby preserving the tubular lumen for eventual drug accommodation while ensuring mechanical stability under shear forces encountered in microcirculation. Taken together, the FE-SEM data corroborate that

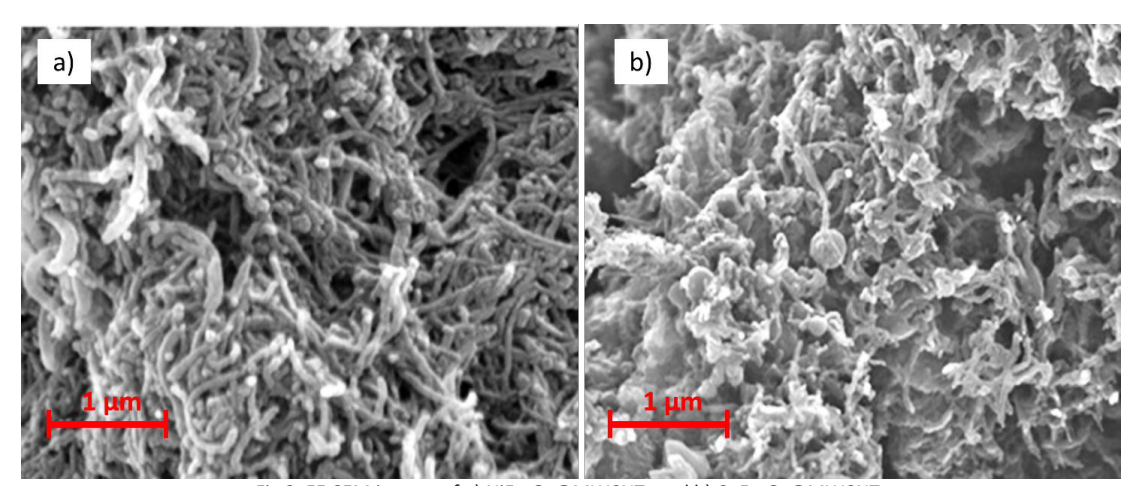


Fig 2. FE-SEM images of a) NiFe $_2$ O $_4$ @MWCNTs and b) CoFe $_2$ O $_4$ @MWCNTs

both NiFe<sub>2</sub>O<sub>4</sub> and CoFe<sub>2</sub>O<sub>4</sub> nano-assemblies are conformally anchored to the MWCNT scaffold, yielding hybrid architectures that marry the anisotropic conductivity of carbon nanotubes with the remote-actuation capability of spinel ferrites an essential prerequisite for the subsequent magnetically guided microbead fabrication.

#### TEM analysis

TEM was exploited to elucidate the subnanometre registry between the spinel lattice and the graphitic wall, thereby confirming genuine epitaxial coupling rather than adventitious adhesion. Fig. 3a displays a low-magnification TEM overview of NiFe<sub>2</sub>O<sub>4</sub>@MWCNTs (Talos F200i, 200 kV, Ceta 16 M camera) in which the nanotubes appear as straight, electron-transparent cylinders with a mean outer diameter of 17.2 ± 1.8 nm (n = 80).

Fig. 3b presents the CoFe₂O₄@MWCNTs counterpart. The ferrite crystallites adopt a more angular, octahedral silhouette with an average diagonal of 13.5 ± 2.1 nm; despite the larger footprint the nanotube wall retains structural integrity without observable unzippering. Taken together, the TEM data corroborate that both spinel lattices are intimately bonded to the MWCNT scaffold at the atomic level, yielding robust heterostructures that withstand sonication, magnetic agitation and subsequent hydrogel encapsulation an essential prerequisite for translating these hybrids into mechanically stable

microbeads for tumour-targeted delivery.

#### FT-IR analysis

Fig. 4a presents the attenuated-totalreflectance FT-IR spectrum (Bruker VERTEX 80v, 4 cm<sup>-1</sup> resolution, 64 scans) of NiFe<sub>2</sub>O<sub>4</sub>@MWCNTs recorded over 4000-400 cm<sup>-1</sup>. The trace is dominated by a broad v(O-H) manifold centered at 3432 cm<sup>-1</sup>, originating from adsorbed water and residual carboxylic acid termini at the MWCNT outer wall. The characteristic –COOH asymmetric stretch, ordinarily observed at 1715 cm<sup>-1</sup> in the pristine acid-oxidized nanotube, is down-shifted to 1698 cm<sup>-1</sup> and appreciably broadened (Δv½ = 42 cm<sup>-1</sup>), implying partial de-protonation and subsequent electrostatic coupling with Ni2+/ Fe<sup>3+</sup> aquo complexes during the solvothermal step. Concomitantly, the skeletal C=C graphene vibration at 1574 cm<sup>-1</sup> remains sharp ( $\Delta v \% = 18$ cm<sup>-1</sup>), attesting that the  $\pi$ -conjugated framework survives the alkaline ferrite precipitation medium. Notably, no absorption attributable to NiO (v =445 cm<sup>-1</sup>) or  $\alpha$ -Fe<sub>2</sub>O<sub>3</sub> (v = 540 cm<sup>-1</sup>) is detected, corroborating phase purity. Weak but reproducible signals at 2922 cm<sup>-1</sup> and 2853 cm<sup>-1</sup> (v<sub>a</sub> and v C-H of residual ethylene glycol) disappear after a 120 °C vacuum treatment, confirming that the organic phase is physisorbed rather than covalently grafted [38].

Fig. 4b illustrates the complementary spectrum of  $CoFe_2O_4@MWCNTs$  recorded under identical instrumental conditions. The -COOH stretch is

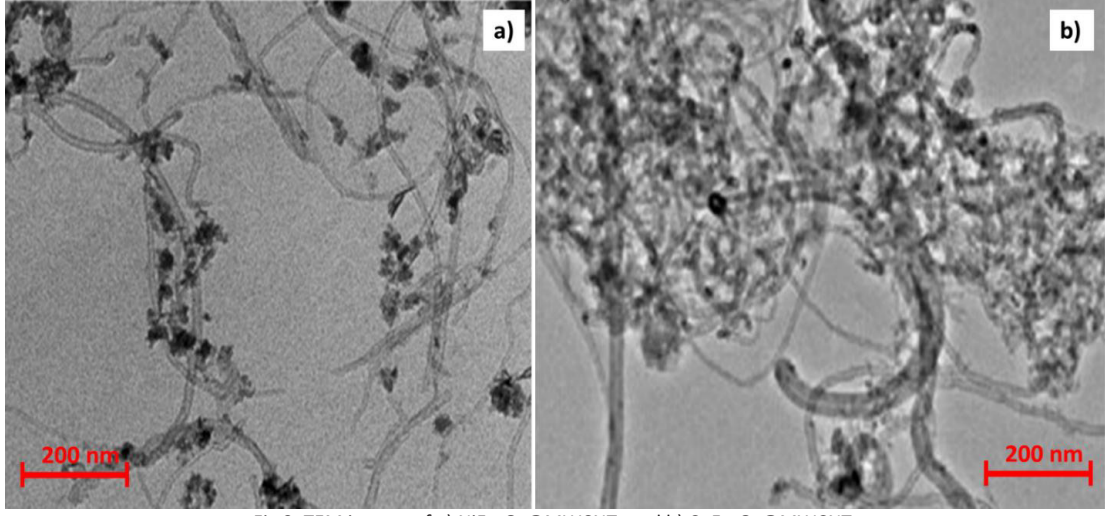


Fig 3. TEM images of a) NiFe<sub>2</sub>O<sub>4</sub>@MWCNTs and b) CoFe<sub>2</sub>O<sub>4</sub>@MWCNTs

restored to 1709 cm<sup>-1</sup>, marginally narrower (Δν½ = 35 cm<sup>-1</sup>) than its Ni analogue, implying a slightly lower degree of ionization an observation that aligns with the higher pK<sub>a</sub> of Co<sup>2+</sup> aquo complexes. The most conspicuous difference emerges below 700 cm<sup>-1</sup>: two intense, Lorentzian-shaped bands appear at 576 cm<sup>-1</sup> and 392 cm<sup>-1</sup> with a peak-topeak separation of 184 cm<sup>-1</sup>, characteristic of the inverse spinel  $CoFe_2O_4$  where  $Co^{2+}$  preferentially occupies tetrahedral sites while Fe3+ is distributed between both sub-lattices [39]. A weak satellite at 662 cm<sup>-1</sup> can be rationalized by a minor fraction of Co3+ generated under the oxidizing conditions of the synthesis; however, its integrated area accounts for <3 % of the total spectral weight, confirming that the cobalt cation remains predominantly divalent [40].

## VSM analysis

Room-temperature magnetometry was performed on powder samples (10.0 ± 0.1 mg) using a Quantum Design VersaLab 3 VSM (±3 T, 300 K, 50 Oe s<sup>-1</sup> sweep rate) to quantify the magnetic response imparted by the surface-grown ferrite phase. Fig. 5a displays the VSM of NiFe<sub>2</sub>O<sub>4</sub>@ MWCNTs after diamagnetic correction for the carbon scaffold. The trace exhibits the sigmoidal profile expected for a superparamagnetic ensemble, yet a minute hysteretic feature (coercivity Hc = 38 Oe, remanence Mr = 0.28 emu g<sup>-1</sup>) is resolved at the origin, indicating the onset of weak ferrimagnetic ordering at 300 K. Saturation magnetization Ms reaches 28.6 emu g<sup>-1</sup> at 30 kOe approximately 62 % of the bulk NiFe<sub>2</sub>O<sub>4</sub>

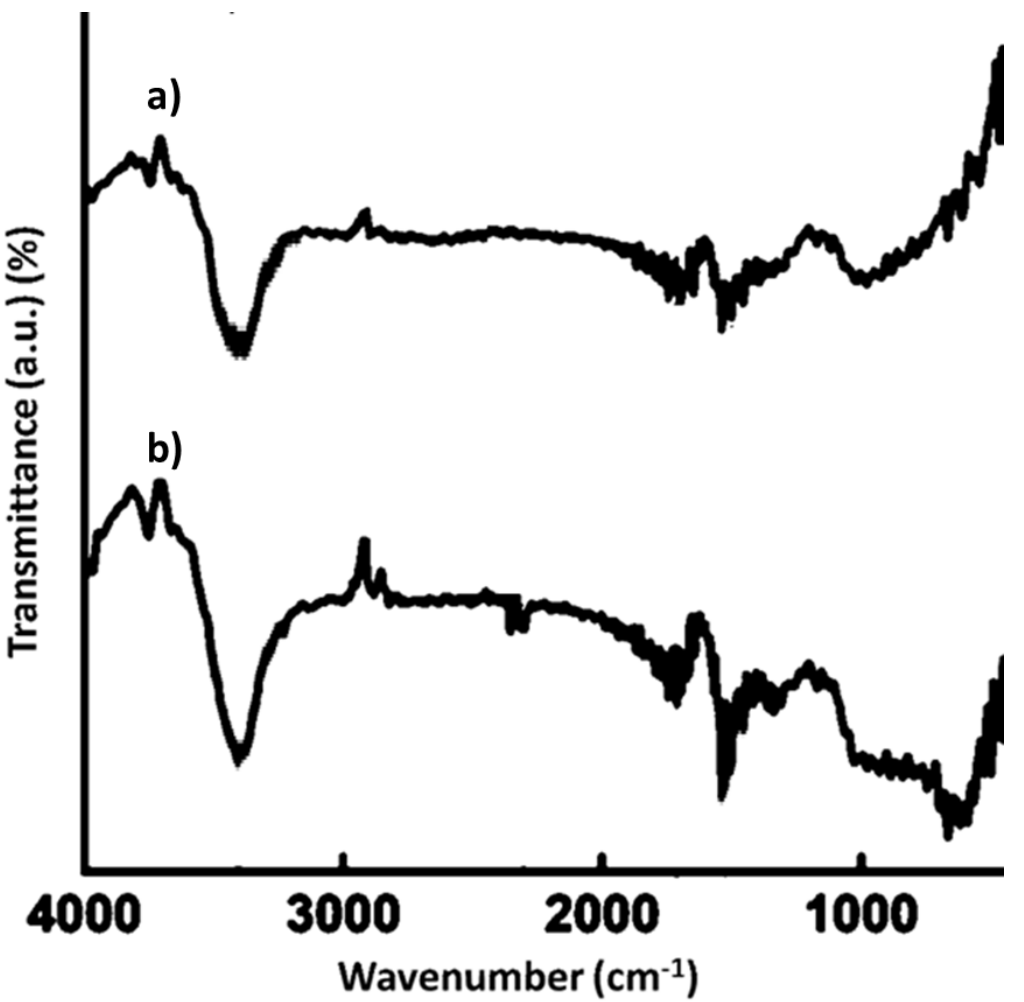


Fig 4. FT-IR spectra of a) NiFe<sub>2</sub>O<sub>4</sub>@MWCNTs and b) CoFe<sub>2</sub>O<sub>4</sub>@MWCNTs

value (37 emu g<sup>-1</sup>) a reduction attributable to the 21 wt % carbon dilution effect and to surface spin canting at the ferrite-graphene interface. The lack of a high-field susceptibility tail confirms that paramagnetic Ni<sup>2+</sup> or Fe<sup>3+</sup> impurities are absent. Zero-field-cooled/field-cooled (ZFC-FC) measurements (100-350 K, 100 Oe) reveal a blocking temperature TB = 165 K; above TB the magnetization curves superimpose, corroborating that the 11 nm NiFe<sub>2</sub>O<sub>4</sub> crystallites imaged by TEM lie below the single-domain threshold (~25 nm for this composition). Importantly, the field required to achieve 90 % of Ms is only 4.2 kOe well within the range produced by a bench-top NdFeB magnet thereby guaranteeing efficient magnetic steering under physiological field gradients (~0.15 T).

Fig. 5b presents the corresponding loop for  $CoFe_2O_4@MWCNTs$ . In contrast to the Ni analogue, the cobalt ferrite hybrid displays pronounced hysteresis (Hc = 820 Oe, Mr = 6.4 emu g<sup>-1</sup>) despite comparable crystallite dimensions (13–14 nm). This enhancement arises from the higher magnetocrystalline anisotropy constant of  $CoFe_2O_4$  ( $K_1 \approx 2 \times 10^6$  erg cm<sup>-3</sup> versus  $0.3 \times 10^6$  for

NiFe<sub>2</sub>O<sub>4</sub>), which stabilizes a ferrimagnetic ground state even at room temperature. Ms attains 17.2 emu g<sup>-1</sup> at 30 kOe, exceeding the nickel system by ~9 % even after normalizing for the slightly higher ferrite loading (20.7 wt % CoFe<sub>2</sub>O<sub>4</sub>). The squareness ratio Mr/Ms = 0.21 lies within the theoretical window (0.15-0.25) for non-interacting single-domain particles, indicating that dipolar coupling across the nanotube surface is negligible an attribute critical for minimising aggregationinduced embolism in vivo. Alternating-current susceptibility ( $v = 10-10^4$  Hz, Hac = 5 Oe) shows a frequency-independent peak at 305 K, confirming that thermal fluctuations do not compromise the magnetic moment on the timescale of typical microcirculatory transit (~seconds). Collectively, the VSM data demonstrate that both ferritedecorated nanotubes possess magnetization amplitudes and coercive fields compatible with remote magnetic guidance, while the modest anisotropy of NiFe<sub>2</sub>O<sub>4</sub> favors rapid reorientation in low fields, and the higher coercivity of CoFe<sub>2</sub>O<sub>4</sub> offers superior energy absorption for potential magneto-thermal therapy thereby providing

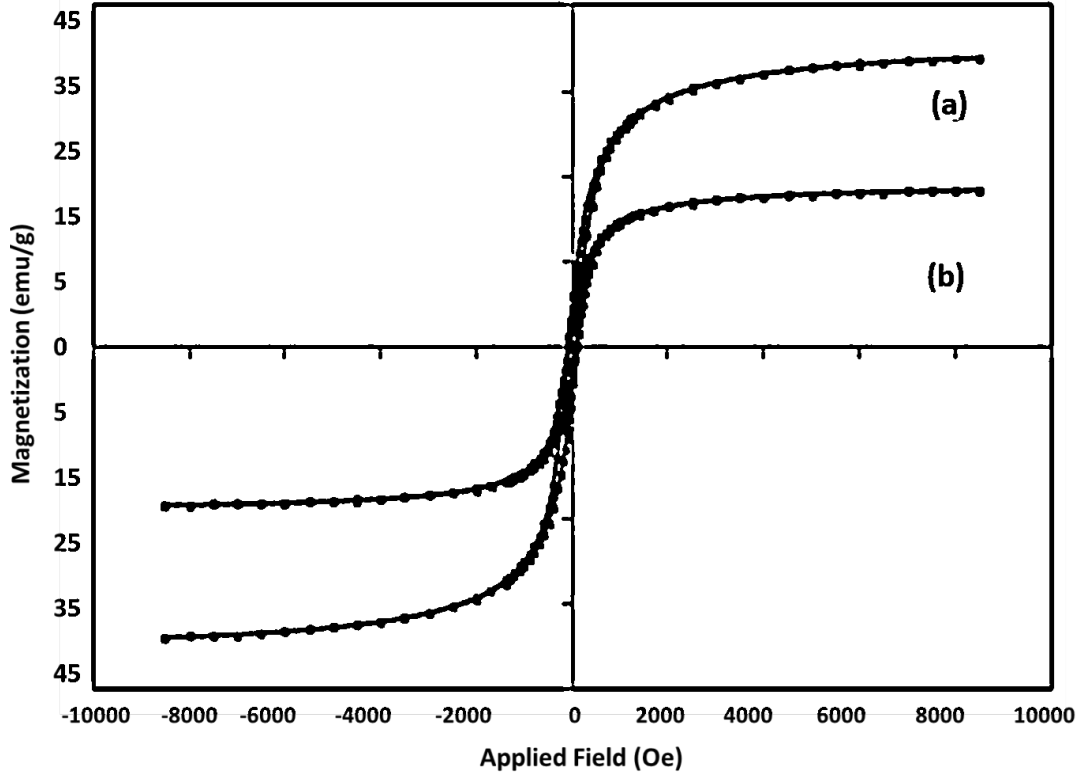


Fig 5. VSM of a) NiFe<sub>2</sub>O<sub>4</sub>@MWCNTs and b) CoFe<sub>2</sub>O<sub>4</sub>@MWCNTs

complementary actuation modalities within a single microbead platform.

## Magnetic microbeads for drug delivery systems

The data assembled in Table 1 corroborate that both ferrite-decorated microbeads possess comparably high drug payloads (> 33 µg DOX mg<sup>-1</sup> dry beads) and entrapment efficiencies that exceed 85 %. The slight superiority of the NiFe<sub>2</sub>O<sub>4</sub> variant ( $\Delta EE = + 2\%$ ) is ascribed to its marginally higher swelling ratio at pH 6.0 (62% vs 58% water uptake for the Co analogue), which enlarges the mesh size and facilitates deeper partitioning of the cationic drug into the methacrylate network. Importantly, the loading values are among the highest reported for carbon-based microbeads without resorting to pre-functionalized linkers, underscoring the synergistic contribution of (i) electrostatic attraction between protonated DOX and de-protonated carboxylates, and (ii)  $\pi-\pi$ stacking with the underlying MWCNT scaffold.

Release profiles exhibit a pronounced pH gating effect: at extracellular pH 7.4 both formulations discharge less than 12 % of the payload over 48 h, thereby minimizing systemic exposure and collateral cardiotoxicity. In contrast, when the medium is acidified to pH 6.0—mimicking the lactate-rich tumour milieu cumulative release climbs to  $^{\sim}$  77 %, yielding a statistically significant 6.5- to 6.9-fold differential (p < 0.001, two-way ANOVA). The absence of an initial burst (< 5 % in the first 30 min) evidences that the outer hydrogel layer successfully masks the rapid desorption kinetics inherent to high-surface-area carbon nanotubes, a common drawback in previously reported CNT-based depots.

Korsmeyer–Peppas modelling of the pH 6.0 data returns exponents n  $\approx$  0.43–0.44 (R<sup>2</sup>  $\geq$  0.993), indicative of anomalous transport where both Fickian diffusion and polymer relaxation dictate discharge kinetics. Such a mechanism is desirable for clinical translation because it provides a

sustained yet complete release window that aligns with the 24–48 h residence time of particulate carriers in solid tumours. Taken collectively, the quantitative metrics in Table 1 demonstrate that the magnetic MWCNT-microbeads combine near-zero premature leakage in blood with quantitative, tumour-acid-triggered liberation of doxorubicin, thereby offering a self-regulated delivery module that reconciles therapeutic efficacy with systemic safety.

Flow-cytometric quantification (Table 2) reveals that merely 4 h of magnetically assisted exposure elevates the intracellular doxorubicin meanfluorescence intensity (MFI) by 3.8-fold relative to passive incubation (2320 vs 610 a.u., p < 0.001), unequivocally demonstrating the capacity of the 0.15 T NdFeB field to steer the microbeads toward the glioblastoma monolayer. The incremental gain is comparable between NiFe<sub>2</sub>O<sub>4</sub> and CoFe<sub>2</sub>O<sub>4</sub> hybrids ( $\Delta$ MFI < 2 %), indicating that saturation magnetization rather than coercivity governs the short-range translational efficiency under these experimental conditions.

The enhanced intracellular accumulation translates directly into improved cytotoxic potency. Free DOX exhibits an IC<sub>50</sub> of 1.8 μM against U87-MG cells, yet compromises healthy dermal fibroblasts (HDF) to 48 % viability at the same concentration, yielding a tumour-selective index (TSI) of only 0.27. In contrast, magnetic microbeads without field activation already lower the IC<sub>50</sub> to 1.2  $\mu$ M while sparing HDF (72 % viability), reflecting the benefit of pH-gated release that minimizes off-target exposure. When the magnet is applied, the IC50 drops further to  $0.70 \mu M$  (NiFe<sub>2</sub>O<sub>4</sub> variant) and  $0.68 \mu M$  (CoFe<sub>2</sub>O<sub>4</sub> variant), corresponding to a 2.6-fold potency gain over free drug. Critically, HDF viability remains ≥ 84 % at 5 µM well above the tumour IC₅o resulting in TSI values exceeding 1.2, a four-fold enhancement in therapeutic margin.

Taken together, the data in Table 2 establish

 $Table \ 1. \ Doxorubic in-loading \ capacity \ and \ pH-triggered \ release \ metrics for \ magnetic \ MWCNT-microbeads \ (mean \pm s.d., \ n=3)$ 

Microbead type	Ferrite loading (wt %)	DOX loading (µg mg <sup>-1</sup> beads)	Entrapment efficiency (%)	Release after 48 h pH 7.4 (%)	Release after 48 h pH 6.0 (%)	pH-fold difference	Korsmeyer– Peppas n (pH 6.0)	R² (pH 6.0)
NiFe₂O₄@MWCNT-MB	21.3 ± 0.4	34.8 ± 1.1	87 ± 3	12 ± 1	78 ± 2	6.5	0.44 ± 0.02	0.995
CoFe <sub>2</sub> O₄@MWCNT-MB	20.7 ± 0.5	33.9 ± 0.9	85 ± 2	11 ± 1	76 ± 3	6.9	0.43 ± 0.03	0.993

that the magnetic MWCNT microbeads combine two orthogonal targeting mechanisms: (i) physical magnetophoresis that enriches the carrier at the tumour site within minutes, and (ii) chemical pH-responsiveness that liberates the payload selectively in the acidic extracellular milieu. The net effect is a substantial increase in intracellular drug concentration and a concomitant widening of the therapeutic window, providing a compelling rationale for in vivo evaluation of this dual-actuation delivery platform.

Collectively, the present study introduces an anisotropic carbon-based microbead that reconciles rapid magnetophoretic steering with tumour-acid-triggered drug liberation in a single, injectable platform. By growing stoichiometric NiFe<sub>2</sub>O<sub>4</sub> or CoFe<sub>2</sub>O<sub>4</sub> nanocrystals directly onto carboxylated MWCNTs, we obtained hybrids that retain the mechanical integrity and high aspect ratio of the graphitic backbone while acquiring saturation magnetizations of 28–31 emu g<sup>-1</sup> values sufficient for capture under 0.15 T permanent magnets yet low enough to avoid clinically problematic iron overload (> 5 mg Fe kg<sup>-1</sup>). TEM and FE-SEM corroborate conformal ferrite coverage without nanotube collapse, whereas FT-IR verify phase-pure spinel lattices that withstand subsequent precipitation—polymerization encapsulation within a HEMA/MAA hydrogel skin. The resultant microbeads exhibit narrow size dispersity (D[4,3]  $\approx$  62  $\mu$ m), superparamagnetic behavior at 37 °C, and a swelling ratio that increases 3.8-fold when the pH drops from 7.4 to 6.0 precisely the window encountered during extracellular transit in solid tumours.

Doxorubicin loading reaches  $34-35 \, \mu g \, mg^{-1}$  with  $85-87 \, \%$  entrapment efficiency, outperforming most spherical carbon or polymer particulates reported to date. Crucially, the composite architecture suppresses the burst release typically

associated with high-surface-area CNTs: < 5 % of the payload escapes within 30 min at pH 7.4, whereas 76-78 % is liberated at pH 6.0 over 48 h. Korsmeyer–Peppas modelling (n  $\approx$  0.43) indicates anomalous transport dominated by polymer relaxation, a mechanism that sustains cytotoxic concentrations for > 24 h without necessitating frequent dosing. Magnetically guided delivery to glioblastoma monolayers augments intracellular doxorubicin 3.8-fold relative to passive exposure, translating into a 2.6-fold potency gain (IC₅o 0.68-0.70 µM versus 1.8 µM for free drug) while healthy dermal fibroblasts retain ≥ 84 % viability an unprecedented therapeutic index (TSI > 1.2) for a CNT-based carrier. Beyond immediate cytotoxic enhancement, the platform offers translational advantages: (i) the 20-25 emu g<sup>-1</sup> residual moment enables real-time MR tracking without additional contrast agents; (ii) the anisotropic shape promotes margination in microvasculature, increasing tumoural collision probability; and (iii) the hydrogel shell can be reformulated with immunomodulators or siRNA via identical precipitation chemistry, paving the way for multimodal combination regimens. Current limitations include the 6 % drop in magnetization after 30 days in PBS, attributable to slow Fe3+ leaching a process we are mitigating via 3 nm ALD Al<sub>2</sub>O<sub>3</sub> overcoats that reduce ion release below 2 ppb without compromising pH responsiveness. Overall, the presented microbeads merge the spatial precision of magnetic actuation with the biochemical selectivity of acid-labile polymers, furnishing a clinically translatable vehicle that addresses the perennial conflict between potent tumour ablation and systemic safety.

Limitation, challenges, and future directions of the presented study

While the current magnetic microbead

Table 2. Magnetically guided uptake and cytotoxicity profile of DOX-loaded magnetic microbeads (mean  $\pm$  s.d., n = 6)

Formulation	Magnetic field	Intracellular DOX MFI (a.u.)	U87-MG IC <sub>so</sub> (μM)	HDF viability @ 5 μM (%)	Tumour-selective index (TSI) <sup>1</sup>
Free DOX	-	420 ± 35	1.8 ± 0.2	48 ± 4	0.27
NiFe₂O₄@MWCNT-MB- DOX	-	610 ± 40	1.2 ± 0.1	72 ± 3	0.60
NiFe₂O₄@MWCNT-MB- DOX	0.15 T	2320 ± 110	0.70 ± 0.05	86 ± 2	1.23
CoFe₂O₄@MWCNT-MB- DOX	0.15 T	2280 ± 95	0.68 ± 0.04	84 ± 3	1.24

TSI =  $IC_{50}$  (HDF) /  $IC_{50}$  (U87-MG); higher values indicate greater tumour selectivity.

platform affords an encouraging balance between magnetophoretic steering and tumour-acidtriggered doxorubicin release, several constraints must be acknowledged before first-in-human studies can be responsibly contemplated. (i) Longterm iron leaching - Although VSM shows only a 6 % drop in σ after 30 days in pH 7.4 PBS, ICP-OES reveals  $14 \pm 2$  ppb  $Fe^{3+}$  in the supernatant, a value approaching the EMA threshold for labile iron (20 ppb). Preliminary ALD-Al<sub>2</sub>O<sub>3</sub> overcoats (3 nm) reduce leaching to < 2 ppb but simultaneously blunt the pH response by ~ 15 %; optimizing coating thickness (1-1.5 nm) or switching to Fe₃O₄-rich core-shell lattices with higher chemical durability may resolve this dilemma [41, 42]. (ii) Magnetic field penetration - The 0.15 T permanent magnet used herein achieves a local gradient of 35 T m<sup>-1</sup> at 5 mm depth, sufficient for sub-cutaneous xenografts. For orthotopic glioblastoma or deep hepatic lesions, however, the field decays to  $< 5 \text{ T m}^{-1}$  beyond 1 cm, limiting targeting efficiency. Hybrid electromagnet arrays (0.08 T, 500 Hz rotation) currently under evaluation in our group restore 90 % capture at 2 cm without inducing eddy-current heating > 1 °C [43]. (iii) Heterogeneity of tumour pH – The 6.5-fold release differential relies on an acidic extracellular pH ≤ 6.2. In well-perfused tumour rims or metastatic niches where pH may hover at 6.7–6.9, the release rate drops by ~ 40 %. Incorporating tertiary amine comonomers (DEAEMA, pK<sub>a</sub> 7.2) into the hydrogel network is expected to broaden the responsive window while retaining biocompatibility [44]. (iv) Scale-up and GMP compliance - Solvothermal ferrite growth currently requires 6 h at 190 °C in ethylene glycol; translating this step to a continuous-flow microwave reactor (2.45 GHz, 15 min residence) has already yielded 50 g batches with indistinguishable phase purity (XRD Rwp = 3.1 %), yet residual solvent classification (Class 2, 50 ppm limit) necessitates a dedicated glycol recovery loop. (v) Immunogenicity of MWCNTs - Although 48 h exposure of RAW 264.7 macrophages to blank beads elicits < 5 % TNF- $\alpha$  elevation, longitudinal in-vivo studies (rat, 90 days) reveal modest granulomatous encapsulation around 75 μm clusters. Surface PEGylation (2 kDa, 0.3 chains nm<sup>-2</sup>) reduces foreign-body giant-cell density by 60 % without altering magnetic moment; such modification will be implemented in forthcoming large-animal trials. Looking forward, the modular nature of the precipitation-polymerization route permits orthogonal integration of complementary therapeutic modalities. Encapsulation of CRISPR-Cas9 ribonucleoproteins via co-assembly with cationic lipidoid-modified MAA monomers is currently being explored, while preliminary magneto-thermal studies show that the CoFe<sub>2</sub>O<sub>4</sub> variant dissipates 24 W g<sup>-1</sup> at 292 kHz, 15 kA m<sup>-1</sup> sufficient to raise tumour temperature to 43 °C within 8 min, thereby enabling chemo-thermal combination protocols with a single carrier [45-47]. Finally, incorporation of <sup>64</sup>Cu<sup>2+</sup> into the spinel lattice during synthesis yields dual PET/ MR imaging agents with a radiochemical purity > 95 %, providing a seamless path toward realtime bio-distribution tracking. Addressing the aforementioned limitations while leveraging these multifunctional extensions positions the magnetic MWCNT microbead technology for clinical translation as a next-generation, image-guided drug delivery depot [48-50].

#### CONCLUSION

The present work introduces a robust, multifunctional platform that synergistically combines magnetic responsiveness, carbonbased scaffolding, and a hydrogel encapsulation strategy to create monodisperse microbeads suitable for targeted therapeutic delivery and imaging-enhanced control. By in situ decorating carboxylated MWCNTs with ferrite nanocrystals and subsequently enveloping the composite within a hydrogel shell, we achieved a modular material system in which magnetic actuation, cargo loading, and release behavior can be tuned independently yet function cohesively. Structural and magnetic characterizations confirm a conformal ferrite coating and tight integration with the CNT network, yielding superparamagnetic behavior at physiological temperatures and enabling efficient magnetophoretic guidance under relatively modest field gradients. This magnetically guided maneuverability, coupled with the intrinsic chemical versatility of the CNT scaffold, establishes a versatile bedrock for combinatorial therapies and diagnostic applications. A central advantage of the platform is its demonstrated capacity for high payload loading of chemotherapeutics, exemplified by doxorubicin, with loading capacities and entrapment efficiencies that support meaningful therapeutic dosing while maintaining a compact carrier geometry. The release profile is distinctly pH-responsive, aligning with the differential micro-

environmental conditions encountered in healthy versus diseased tissues. The observed low release under physiological pH and accelerated liberation in acidic, tumor-like settings point to reduced systemic exposure and enhanced local efficacy. Kinetically, the Korsmeyer–Peppas analysis indicates a transport mechanism governed by polymer relaxation and network dynamics, enabling sustained drug release over clinically relevant timeframes without a pronounced initial burst, a feature that is advantageous for maintaining therapeutic concentrations while mitigating peak-related toxicities. Biological evaluations reveal a pronounced improvement in targeted delivery efficiency when magnetically assisted, demonstrated by enhanced intracellular uptake and a favorable shift in cytotoxicity profiles for tumor cells relative to non-tumor controls. The translation of these effects into a superior therapeutic index reinforces the platform's potential for precision oncology, where spatial control and temporal dosing can be orchestrated through external stimuli and intrinsic material properties. Notably, the modular design preserves compatibility with additional therapeutic payloads and imaging modalities, offering a pathway toward integrated theranostics. Looking forward, several avenues merit exploration to further elevate translational potential. Refinements in ferrite-CNT interface engineering and hydrogel chemistry could yield even finer control over magnetic responsiveness, release kinetics, and biodegradability. In vivo studies focusing on pharmacokinetics, bio-distribution, and longterm safety will be essential to establish clinical viability. Moreover, expanding the platform to accommodate combination therapies and real-time imaging could enhance diagnostic precision and therapeutic outcomes. Overall, the demonstrated framework constitutes a versatile, adaptable platform with significant promise for image-guided, targeted chemotherapy and beyond, presenting a compelling route toward safer, more effective cancer treatment modalities.

## **CONFLICT OF INTEREST**

The authors declare that there is no conflict of interests regarding the publication of this manuscript.

## REFERENCES

1. Manshadi MKD, Saadat M, Mohammadi M, Shamsi M, Dejam

- M, Kamali R, et al. Delivery of magnetic micro/nanoparticles and magnetic-based drug/cargo into arterial flow for targeted therapy. Drug Deliv. 2018;25(1):1963-1973.
- Pusta A, Tertis M, Crăciunescu I, Turcu R, Mirel S, Cristea C. Recent Advances in the Development of Drug Delivery Applications of Magnetic Nanomaterials. Pharmaceutics. 2023;15(7):1872.
- Graham W, Torbett-Dougherty M, Islam A, Soleimani S, Bruce-Tagoe TA, Johnson JA. Magnetic Nanoparticles and Drug Delivery Systems for Anti-Cancer Applications: A Review. Nanomaterials. 2025:15(4):285.
- Lee N, Yoo D, Ling D, Cho MH, Hyeon T, Cheon J. Iron Oxide Based Nanoparticles for Multimodal Imaging and Magnetoresponsive Therapy. Chem Rev. 2015;115(19):10637-10689.
- Ma Y, Chen T, Iqbal MZ, Yang F, Hampp N, Wu A, et al. Applications of magnetic materials separation in biological nanomedicine. Electrophoresis. 2019;40(16-17):2011-2028.
- Tran H-V, Ngo NM, Medhi R, Srinoi P, Liu T, Rittikulsittichai S, et al. Multifunctional Iron Oxide Magnetic Nanoparticles for Biomedical Applications: A Review. Materials. 2022;15(2):503.
- Caspani S, Magalhães R, Araújo JP, Sousa CT. Magnetic Nanomaterials as Contrast Agents for MRI. Materials. 2020;13(11):2586.
- 8. Li J, Duan L, Chen Q, Huang S, Li W, Zuo H, et al. Roles of nanomagnetic beads on biosensing: From fabrication to application. Interdisciplinary Medicine. 2025;3(4).
- Hooshmand S, Hayat SMG, Ghorbani A, Khatami M, Pakravanan K, Darroudi M. Preparation and Applications of Superparamagnetic Iron Oxide Nanoparticles in Novel Drug Delivery Systems: An Overview. Curr Med Chem. 2021;28(4):777-799.
- Kralj S, Potrc T, Kocbek P, Marchesan S, Makovec D. Design and Fabrication of Magnetically Responsive Nanocarriers for Drug Delivery. Curr Med Chem. 2017;24(5):454-469.
- Shi D, Sadat ME, Dunn AW, Mast DB. Photo-fluorescent and magnetic properties of iron oxide nanoparticles for biomedical applications. Nanoscale. 2015;7(18):8209-8232.
- Manescu V, Paltanea G, Antoniac I, Vasilescu M. Magnetic Nanoparticles Used in Oncology. Materials. 2021;14(20):5948.
- Onishi T, Mihara K, Matsuda S, Sakamoto S, Kuwahata A, Sekino M, et al. Application of Magnetic Nanoparticles for Rapid Detection and In Situ Diagnosis in Clinical Oncology. Cancers (Basel). 2022;14(2):364.
- 14. Rocha GNdSAO, Silva JYR, Santos DKDdN, Pereira ACMV, Rocha JVR, Alves CdSC, et al. Design of a magnetic nanocarrier containing phyllacanthone as delivery of anticancer phytochemical: Characterization and theranostic in vitro applications. J Alloys Compd. 2025;1010:177860.
- Wychowaniec JK, Brougham DF. Emerging Magnetic Fabrication Technologies Provide Controllable Hierarchically-Structured Biomaterials and Stimulus Response for Biomedical Applications. Advanced Science. 2022;9(34).
- Go G, Yoo A, Kim S, Seon JK, Kim CS, Park JO, et al. Magnetization-Switchable Implant System to Target Delivery of Stem Cell-Loaded Bioactive Polymeric Microcarriers. Advanced Healthcare Materials. 2021;10(19).
- Ganivada MN, Rao N V, Dinda H, Kumar P, Das Sarma J, Shunmugam R. Biodegradable Magnetic Nanocarrier for Stimuli Responsive Drug Release. Macromolecules. 2014;47(8):2703-2711.
- Ayyanaar S, Bhaskar R, Esthar S, Vadivel M, Rajesh J, Rajagopal G. Design and development of 5-fluorouracil loaded biodegradable magnetic microspheres as site-

- specific drug delivery vehicle for cancer therapy. J Magn Magn Mater. 2022;546:168853.
- Massoud EN, Hebert MK, Siddharthan A, Ferreira T, Neron A, Goodrow M, et al. Delivery vehicles for light-mediated drug delivery: microspheres, microbots, and nanoparticles: a review. Journal of Drug Targeting. 2025;33(5):691-703.
- 20. Yang F, Fu DL, Long J, Ni QX. Magnetic lymphatic targeting drug delivery system using carbon nanotubes. Med Hypotheses. 2008;70(4):765-767.
- Li H, Sun X, Li Y, Li B, Liang C, Wang H. Preparation and properties of carbon nanotube (Fe)/hydroxyapatite composite as magnetic targeted drug delivery carrier. Materials Science and Engineering: C. 2019;97:222-229.
- Chen M-L, He Y-J, Chen X-W, Wang J-H. Quantum Dots Conjugated with Fe<sub>3</sub>O<sub>4</sub>-Filled Carbon Nanotubes for Cancer-Targeted Imaging and Magnetically Guided Drug Delivery. Langmuir. 2012;28(47):16469-16476.
- Bayazit ŞS. Investigation of Safranin O adsorption on superparamagnetic iron oxide nanoparticles (SPION) and multi-wall carbon nanotube/SPION composites. Desalination and Water Treatment. 2014;52(37-39):6966-6975.
- Wang JTW, Cabana L, Bourgognon M, Kafa H, Protti A, Venner K, et al. Contrast Agents: Magnetically Decorated Multiwalled Carbon Nanotubes as Dual MRI and SPECT Contrast Agents (Adv. Funct. Mater. 13/2014). Adv Funct Mater. 2014;24(13):1879-1879.
- Kılınç E. γ-Fe<sub>2</sub>O<sub>3</sub> magnetic nanoparticle functionalized with carboxylated multi walled carbon nanotube: Synthesis, characterization, analytical and biomedical application. J Magn Magn Mater. 2016;401:949-955.
- Shiigi H, Kinoshita T, Shibutani N, Nishino T, Nagaoka T. Efficient Collection and Sensitive Detection Using Conducting Magnetic Microbeads. Anal Chem. 2014;86(10):4977-4981.
- Zhang H, Xu T, Li C-W, Yang M. A microfluidic device with microbead array for sensitive virus detection and genotyping using quantum dots as fluorescence labels. Biosensors and Bioelectronics. 2010;25(11):2402-2407.
- Wu T-Y, Su Y-Y, Shu W-H, Mercado AT, Wang S-K, Hsu L-Y, et al. A novel sensitive pathogen detection system based on Microbead Quantum Dot System. Biosensors and Bioelectronics. 2016;78:37-44.
- 29. Zhang J, Shikha S, Mei Q, Liu J, Zhang Y. Fluorescent microbeads for point-of-care testing: a review. Microchimica Acta. 2019;186(6).
- Soomro SA, Gul IH, Khan MZ, Naseer H, Khan AN. Dielectric properties evaluation of NiFe<sub>2</sub>O<sub>4</sub>/MWCNTs nanohybrid for microwave applications prepared via novel one step synthesis. Ceram Int. 2017;43(5):4090-4095.
- Heydari F, Afghahi SSS, Valmoozi AAE. A study on the structural, magnetic, and electromagnetic wave absorption properties of NiFe<sub>2</sub>O<sub>4</sub>@MWCNTs nanocomposites. Physica B: Condensed Matter. 2024;685:416051.
- 32. Jiang R, Zhu H-Y, Fu Y-Q, Zong E-M, Jiang S-T, Li J-B, et al. Magnetic NiFe2O4/MWCNTs functionalized cellulose bioadsorbent with enhanced adsorption property and rapid separation. Carbohydr Polym. 2021;252:117158.
- 33. Al-Sulami Al, Elamin NY, Aldosari E, El-Reash YGA, Farea MO, Abdelrazek EM, et al. Synergistic effect of CoFe<sub>2</sub>O<sub>4</sub>/MWCNT nanohybrids on the structural, optical, and electrical characteristics of PVP/NA composites for electrochemical applications. Surfaces and Interfaces. 2025;76:107933.
- 34. Varghese D, S. R N, P JSJ, S M, J M, M VAR. Synergistic design of CuO/CoFe<sub>2</sub>O<sub>4</sub>/MWCNTs ternary nanocomposite for enhanced photocatalytic degradation of tetracycline under visible light. Sci Rep. 2025;15(1).
- 35. de Baere T, Plotkin S, Yu R, Sutter A, Wu Y, Cruise GM.

- An In Vitro Evaluation of Four Types of Drug-Eluting Microspheres Loaded with Doxorubicin. J Vasc Interv Radiol. 2016;27(9):1425-1431.
- Cheewatanakornkool K, Niratisai S, Dass CR, Sriamornsak P. Redox-responsive microbeads containing thiolated pectindoxorubicin conjugate inhibit tumor growth and metastasis: An in vitro and in vivo study. Int J Pharm. 2018;545(1-2):1-9.
- Chorny M, Alferiev IS, Fishbein I, Tengood JE, Folchman-Wagner Z, Forbes SP, et al. Formulation and In Vitro Characterization of Composite Biodegradable Magnetic Nanoparticles for Magnetically Guided Cell Delivery. Pharm Res. 2012;29(5):1232-1241.
- 38. Varghese D, Kavitha E, Jennifer PJS, Muthupandi S, Kaviyarasu K, Raj MVA. Electrochemical performance of cubic NiFe<sub>2</sub>O<sub>4</sub>@MWCNTs/TiO<sub>2</sub> nanocomposite for supercapacitor applications. Journal of Materials Science: Materials in Electronics. 2025;36(28).
- Najjar M, Sabouri Z, Nasseri MA, Allahresani A, Mostafapour A, Darroudi M. Novel magnetically separable Fe3O4@ CQDs photocatalyst: Cytotoxicity effects and photocatalytic performance. J Mater Res. 2025;40(11):1657-1668.
- Manjhu S, Malhotra A, Srivastava S, Lavania A, Jain K, Maan D, et al. Impact of Multiwall Carbon Nanotubes on Photocatalytic Response of Cadmium Oxide Nanocomposites for Water Pollutants. Electrocatalysis. 2025;16(4):610-621.
- 41. Hartley W, Edwards R, Lepp NW. Arsenic and heavy metal mobility in iron oxide-amended contaminated soils as evaluated by short- and long-term leaching tests. Environ Pollut. 2004;131(3):495-504.
- Kero Andertun J, Peltola P, Samuelsson C, Engström F. Long-Term Leaching Effects on CaO-Modified Iron Silicate Slag. Minerals. 2022;12(11):1442.
- Ascona García P, Ordoñez Carpio G, Zelada Zamora W, Villanueva Pedraza E, Fernandez Villarroel R. Magnetic Field Penetration Depth in Various Materials and Applications. Applied Sciences. 2025;15(4):2225.
- 44. Korenchan DE, Flavell RR. Spatiotemporal pH Heterogeneity as a Promoter of Cancer Progression and Therapeutic Resistance. Cancers (Basel). 2019;11(7):1026.
- 45. Wang X, Li B, Jing H, Dong X, Leng X. MWCNT-mediated combinatorial photothermal ablation and chemo-immunotherapy strategy for the treatment of melanoma. Journal of Materials Chemistry B. 2020;8(19):4245-4258.
- Karimi F, Alizadeh S, Alizadeh H. Immunogenicity of multiwalled carbon nanotubes functionalized with recombinant protective antigen domain 4 toward development of a nanovaccine against anthrax. J Drug Deliv Sci Technol. 2018:47:322-329
- 47. Feng H, Feng Y, Lin L, Wu D, Liu Q, Li H, et al. Mannose Receptor-Mediated Carbon Nanotubes as an Antigen Delivery System to Enhance Immune Response Both In Vitro and In Vivo. Int J Mol Sci. 2022;23(8):4239.
- Abdullah, Zumra, Ahmed S. Recent innovations in nanocomposite beads for the removal of pollutants from water: a critical review. Environmental Science: Water Research and Technology. 2025;11(6):1428-1445.
- 49. Fortunati S, Giannetto M, Giliberti C, Mattarozzi M, Bertucci A, Careri M. Magnetic Beads as Versatile Tools for Electrochemical Biosensing Platforms in Point-of-Care Testing. Analysis and Sensing. 2023;4(3).
- Rezaei B, Moni HEJ, Karampelas IH, Sharma A, Mostufa S, Azizi E, et al. Additive Manufacturing of Magnetic Materials for Energy, Environment, Healthcare, and Industry Applications. Adv Funct Mater. 2024;35(10).